$\mathcal{L}_1$ Adaptive Control of Hysteresis in Smart Materials

Xiang Fan* and Ralph C. Smith†

Center for Research in Scientific Computation
Department of Mathematics
North Carolina State University
Raleigh, NC 27695

ABSTRACT

Smart materials display coupling between electrical, magnetic, thermal and elastic behavior. Hence these materials have inherent sensing and actuation capacities. However, the hysteresis inherent to smart materials presents a challenge in control of these actuators/sensors. Inverse compensation is a fundamental approach to cope with hysteresis, where one aims to cancel out the hysteresis effect by constructing a right inverse of the hysteresis. The performance of the inverse compensation is susceptible to model uncertainties and to error introduced by inexact inverse algorithms. We employ a mathematical model for describing hysteresis. On the basis of the hysteresis model, a robust adaptive inverse control approach is presented, for reducing hysteresis. The asymptotic tracking property of the adaptive inverse control algorithm is proved and the issue of parameters convergence is discussed in terms of the reference trajectory. Moreover, sufficient conditions under which parameter estimates converge to their true values are derived. Simulations are used to examine the effectiveness of the proposed approach.

Keywords: smart materials, hysteresis, inverse compensation, $\mathcal{L}_1$ adaptive control

1. INTRODUCTION

The role of smart materials continues to be critical to technology development in many biomedical, aerospace, and industrial applications. These materials provide advantages in applications where large forces and small displacements are desired over a broad frequency range with high precision. A large number of these applications employ piezoelectric or magnetostrictive materials which respectively possess electric or magnetic field induced displacement and force. Although smart materials have been successfully implemented in a number of applications, limitations associated with nonlinear and hysteretic behavior have presented challenges in developing high performance actuation responses over a broad frequency range. The nonlinear and hysteretic behavior is primarily due to the reorientation of local electric or magnetic variants that align with the applied electric or magnetic fields. Moderate to large field levels can induce 0.1% strain in PZT and up to 6% strain in shape memory alloys. At these fields levels, however, obtaining accurate and precise control is greatly complicated by nonlinearities and hysteresis. This has motivated research in developing new control designs that can effectively compensate for nonlinearities and hysteresis induced by ferroelectric or ferromagnetic switching while still providing accurate forces or displacement over a broad frequency range.

Two general strategies are typically considered when developing a control design to compensate for hysteresis. One approach is to implement a nonlinear inverse compensator which approximately linearizes the constitutive behavior so that linear control methods can be employed. This approach provides the ability to implement linear control laws; however, this advantage is only realized if the constitutive model is efficient enough to be inverted in real time. The second strategy entails direct incorporation of the material model into the control design so that the nonlinear control input is directly determined. This circumvents issues associated with computing the constitutive inverse law, but introduces challenges in identifying robust numerical algorithms that can achieve convergence efficiently.

*E-mail: xfan2@ncsu.edu;
†E-mail: rsmith@eos.ncsu.edu, Telephone: 919-515-7552

Both of these approaches require an efficient and accurate constitutive model that can predict the hysteresis behavior. In the analysis presented here, a homogenized model is implemented which utilizes fundamental energy relations at the mesoscopic scale to quantify macroscopic behavior in materials. This modeling framework has been successful in accurately quantifying rate-dependent major an minor hysteresis loops in ferroelectric, magnetostrictive and shape memory alloy; see [4] for details. The first strategy is presented here where the inverse compensator is directly incorporated into the control design.

2. MODEL DEVELOPMENT

The model employed in the present analysis incorporates mesoscopic material behavior at the domain in a stochastic homogenization framework to predict macroscopic material behavior. A distribution of interaction fields and coercive fields is implemented to model polarization switching processes that typically occur in the presence of material in homogeneities and residual fields. Boltzmann relations are included to model thermal relaxation behavior when thermal energy affects polarization switching. Macroscopic material behavior is determined by homogenizing the local polarization variants according to the distribution of interaction and coercive fields.

2.1. Homogenized Energy Model

The equations governing the homogenized energy model are summarized here. A detailed review of the modeling framework is given in [4]. The homogenized energy model is based on an energy description at the mesoscopic length scale. This local energy formulation is used to predict macroscopic behavior using a stochastic representation of material inhomogeneities.

For ferroelectric materials, the Gibbs free energy at the mesoscopic length scale is

$$G = \psi - EP \tag{2.1}$$

where ψ is the Helmholtz energy approximated by the piecewise quadratic function

$$\psi(P) = \begin{cases} \eta(P + P_R)^2/2, & P \leq -P_I \\ \dfrac{\eta}{2}(P_I - P_R)\left(\dfrac{P^2}{P_I} - P_R\right), & |P| < P_I \\ \eta(P - P_R)^2/2, & P \geq P_I \end{cases} \tag{2.2}$$

Here E is the electric field, P is the polarization, P_I denotes the positive inflection point at which the switch occurs, P_R is the local remanence polarization and η is the reciprocal slope $\frac{\partial E}{\partial P}$. The one-dimensional Helmholtz energy function is double-well potential below the Curie point T_c which gives rise to a stable spontaneous polarization with equal magnitude in the positive and negative directions. More details can be found in [4].

The Boltzmann relation gives rise to the local expected values

$$\langle P_+ \rangle = \frac{\int_{P_I}^{\infty} \exp(-G(E + E_I, P)V/kT)dP}{\int_{P_I}^{\infty} P \exp(-G(E + E_I, P)V/kT)dP} \tag{2.3}$$

$$\langle P_- \rangle = \frac{\int_{-\infty}^{-P_I} \exp(-G(E + E_I, P)V/kT)dP}{\int_{\infty}^{-P_I} P \exp(-G(E + E_I, P)V/kT)dP} \tag{2.4}$$

of the polarization associated with positive and negatively oriented dipoles, respectively. Here V is the volume of the mesoscopic layer, k is Boltzmann's constant, and T is the temperature.

The local polarization variants are defined by a volume fraction of variants x_+ and x_- having positive and negative orientations, respectively. The relation $x_- + x_+ = 1$ must hold for the volums fraction of polarization variants.

The resulting local average polarization is qualified by the relation

$$\overline{P} = x_+\langle P_+\rangle + x_-\langle P_-\rangle. \tag{2.5}$$

The macroscopic polarization is computed from the distribution of local variants from the relation

$$[P(E)](t) = \int_{-\infty}^{\infty}\int_{0}^{\infty} \nu_c(E_c)\nu_I(E_I)\overline{P}(E + E_I; E_c; x_+)dE_I dE_c \tag{2.6}$$

where $\nu(E_c)$, $\nu(E_I)$ respectively denote the distributions of coercive field value E_c (at which a dipole changes its orientations) and interaction field value E_I, x_+ represents the distribution of the local variants. The densities can often be modeled as lognormal or normal distributions. However, when more accurate model predictions are critical, a general density can be fit to data. As detailed in [4], the model for magnetic material is equivalent.

2.2. Inverse Compensator

As discussed in Section 1, one method to accurately control a smart material actuator involves the use of an inverse compensator. A prototypical setup for this type for control is depicted in Figure 1. The material is nonlinear, hysteretic, and time-varying, but these attributes are approximately linearized by the inverse filter $\widehat{\mathcal{H}}^{-1}$. The composite system to be controlled is then approximately linear and time-invariant. This allows simple control designs to be utilized, including the $\mathcal{L}_1$ control method employed later.

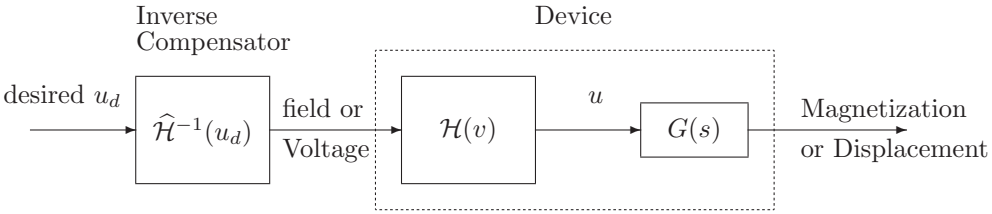

Figure 1. Plant with an input nonlinearity.

The inverse compensator is the inverse of the homogenized energy model. Given a value for the polarization (or magnetization), we want to determine the field level necessary to bring the actuator to that value. More precisely, given any valid state x_+ and any $\widehat{P}$ within the operating range of the material, determine E such that $P = \widehat{P}$, where P is the solution of (2.6). Due to the nonlinearity and dependence on x_+, it is not feasible to invert (2.6) analytically. Thus, the problem is reformulated as a numerical root finding problem, namely determining the value E such that for a given x_+ and $\widehat{P}$,

$$P(E;\, x_+) - \widehat{P} = 0, \tag{2.7}$$

more details can be found in [1].

3. $\mathcal{L}_1$ CONTROL ARCHITECTURE

Consider the system dynamic:

$$\begin{aligned} \dot{\mathbf{x}}(t) &= \mathbf{A}\mathbf{x}(t) + \mathbf{b}u(t), \quad \mathbf{x}(t_0) = \mathbf{x}_0 \\ y(t) &= \mathbf{c}^T\mathbf{x}(t) \end{aligned} \tag{3.1}$$

where $\mathbf{x} = [x,\, \dot{x}]^T$ is the system state vector.

Note that$\mathbf{A}$ may be unknown and we assume that there exists a Hurwitz $\mathbf{A}_m \in \mathbb{R}^{n\times n}$ and a vector of ideal parameter $\theta \in \mathbb{R}^n$ such that $(\mathbf{A}_m,\, \mathbf{b})$ is controllable and $\mathbf{A} - \mathbf{A}_m = \mathbf{b}\,\theta^T$. We further assume the unknown

parameter θ belongs to a given compact convex set Θ. The signal $u(t) = [\mathcal{H}(v)](t)$ includes the output of the inverse compensator where $v(t)$ is defined as the electric field; i.e.,

$$u = [\mathcal{H}(v)](t) = [\mathcal{H}\widehat{\mathcal{H}}^{-1}(u_d)](t) \tag{3.2}$$

where signal $u_d(t)$ is used as the input of the inverse compensator $\widehat{\mathcal{H}}^{-1}(\cdot)$ to generate the control $v(t)$ which is then applied to the device, as shown in Fig. 1.

Since the hysteresis inverse $[\widehat{\mathcal{H}}^{-1}(u_d)](\mathrm{t})$ can not exactly approximate the real inverse of $[\mathcal{H}(v)](t)$, we can write

$$u(t) = u_d(t) + \sigma(t) \tag{3.3}$$

where $\sigma(t)$ is the inversion error introduced by the inverse compensator. Note that the inversion error can be bounded in magnitude; i.e., $|\sigma(t)| \leq \Delta_0 \in \mathbb{R}$. Hence we can model the inversion error as an external disturbance and attenuate its impact by robust control techniques.

Substituting (3.3) into (3.1) yields

$$\begin{aligned} \dot{\mathbf{x}}(t) &= \mathbf{A}_m\mathbf{x}(t) + \mathbf{b}(u_d(t) + \theta^T\mathbf{x}(t) + \sigma(t)), \\ y(t) &= \mathbf{c}^T\mathbf{x}(t). \end{aligned} \tag{3.4}$$

The objective is to design a low-frequency adaptive controller $u_d(t)$ such that $y(t)$ tracks a given bounded reference signal $r(t)$ while all other error signals remain bounded.

The elements of the $\mathcal{L}_1$ adaptive controller are introduced next.

State Predictor: Consider the state predictor

$$\begin{aligned} \dot{\hat{\mathbf{x}}}(t) &= \mathbf{A}_m\hat{\mathbf{x}}(t) + \mathbf{b}(u_d(t) + \hat{\theta}^T\mathbf{x}(t) + \hat{\sigma}(t)), \\ \hat{y}(t) &= \mathbf{c}^T\hat{\mathbf{x}}(t). \end{aligned} \tag{3.5}$$

which has the same structure as the system in (3.4). The only difference is that the unknown parameters $\theta(t)$, $\sigma(t)$ are replaced by their adaptive estimated $\hat{\theta}(t)$, $\hat{\sigma}(t)$ that are governed the following adaptation laws.

Adaptive Laws: Adaptive estimates are defined via the projection operator:

$$\begin{aligned} \dot{\hat{\theta}}(t) &= \Gamma_c\mathrm{Proj}\left(\hat{\theta}(t),\, -\mathbf{x}(t)\tilde{\mathbf{x}}^T(t)Pb\right), && \hat{\theta}(0) = 0 \\ \dot{\hat{\sigma}}(t) &= \Gamma_c\mathrm{Proj}\left(\hat{\sigma}(t),\, -\tilde{\mathbf{x}}^T(t)Pb\right), && \hat{\sigma}(0) = 0 \end{aligned} \tag{3.6}$$

where $\tilde{\mathbf{x}}(t) = \hat{\mathbf{x}}(t) - \mathbf{x}(t)$ is the error between the states of the system and the predictor, P is the solution of the algebraic Lyapunov equation $\mathbf{A}_m^TP + P\mathbf{A}_m = -Q$, $Q > 0$.

Control Law: The control signal $u_d(t)$ is generated through gain feedback of the system

$$\mathcal{X}(s) = D(s)\bar{r}(s), \quad u_d(s) = -k\mathcal{X}(s), \tag{3.7}$$

where $k \in \mathbb{R}^+$ is a feedback gain, $\bar{r}(s)$ is the Laplace transformation of

$$\bar{r}(t) = u_d(t) + \hat{\theta}^T\mathbf{x}(t) + \hat{\sigma}(t) - k_gr(t), \qquad k_g = -\frac{1}{\mathbf{c}^T\mathbf{A}_m^{-1}\mathbf{b}} \tag{3.8}$$

and $D(s)$ is a transfer function that leads to strictly proper stable

$$C(s) = \frac{kD(s)}{1 + kD(s)} \tag{3.9}$$

with low-pass gain $C(0) = 1$.

$\mathcal{L}_1$-gain stability requirement: Design $D(s)$ and k to satisfy

$$\|\bar{G}(s)\|_{\mathcal{L}_1} L < 1, \qquad L = \max_{\theta \in \Theta} \sum_{i=1}^{n} |\theta_i(t)| \tag{3.10}$$

where $\overline{G}(s) = (s\mathbb{I} - \mathbf{A}_m)^{-1} b(1 - C(s))$, and $\mathcal{L}_1$ gain for a stable proper m input n output transfer function, say $G(s)$, is defined as

$$\|G(s)\|_{\mathcal{L}_1} = \max_{i=1,\cdots,n} \left(\sum_{j=1}^{m} \int_0^\infty |g_{ij}(t)| dt \right)$$

where $g_{ij}(t)$ is the impulse response of $G_{ij}(s)$, the i^{th} row j^{th} column element of $G(s)$.

In case of of constant $\theta(t)$, the stability requirement can be simplified. For the specific choice of $D(s) = 1/s$, which yields $C(s) = \dfrac{k}{s+k}$, the stability requirement is reduced to

$$A_g = \begin{bmatrix} \mathbf{A}_m + \mathbf{b}\,\theta^T & \mathbf{b} \\ -k\theta^T & -k \end{bmatrix}$$

being Hurwitz for all $\theta \in \Theta$.

The close-loop system with it is illustrated in Figure 2.

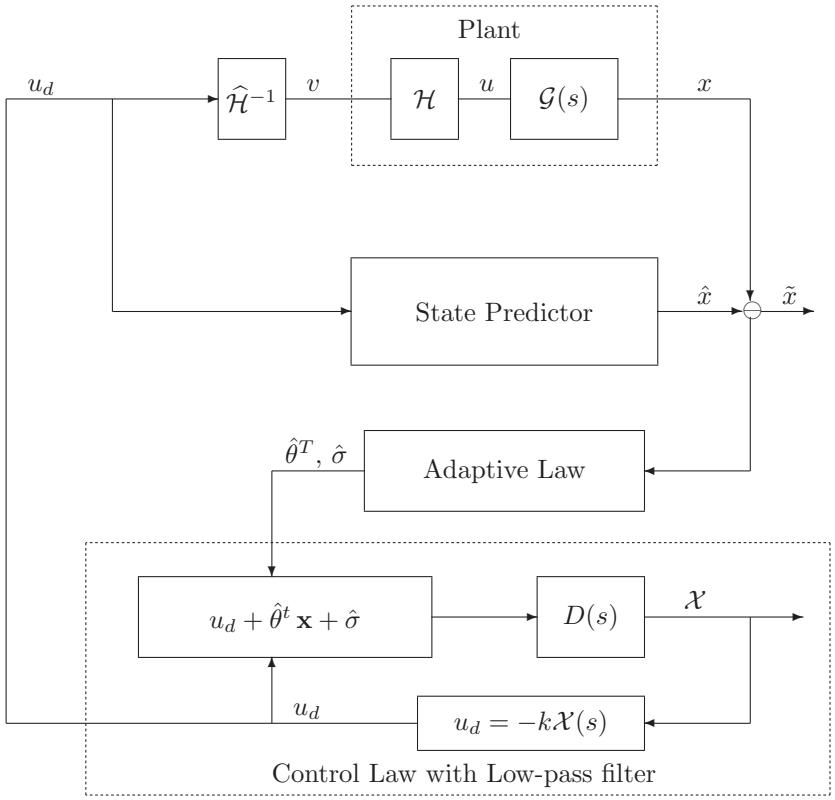

Figure 2. Closed-loop system with the $\mathcal{L}_1$ adaptive controller.

Note that when $C(s) = 1$, u_d reduces to the ideal control signal

$$u_{id}(t) = k_g r(t) - \theta^T \mathbf{x}_{id} - \sigma(t) \tag{3.11}$$

and (3.11) is the one that leads to desired system response

$$\dot{\mathbf{x}}_{id}(t) = \mathbf{A}_m \mathbf{x}_{id}(t) + \mathbf{b} k_g r(t) \tag{3.12}$$

by canceling the uncertainties exactly. In the closed-loop predictor system $(3.5) - (3.7)$, $u_{id}(t)$ is further low-pass filtered by $C(s)$ in (3.9) to have guaranteed low-frequency range. Thus, the system in $(3.5) - (3.7)$ has a different response as compared to (3.12) achieved with (3.11). It has been proved in [2] that the response of the state predictor (3.6) can be made as close as possible to the response of the ideal system (3.12) by reducing $\|\bar{G}(s)\|_{\mathcal{L}_1}$ arbitrarily small, and $\|\bar{G}(s)\|_{\mathcal{L}_1}$ can be made arbitrarily small by appropriately choosing the design constants, further details may be found in [2] and [3].

4. SIMULATION

Consider the dynamic system in (3.1) with $A = \begin{bmatrix} 0 & 1 \\ 5 & 7 \end{bmatrix}$, $b = \begin{bmatrix} 0 \\ 1 \end{bmatrix}$, $c = \begin{bmatrix} 1 \\ 0 \end{bmatrix}$ and the state predictor in (3.5) with $A_m = \begin{bmatrix} 0 & 1 \\ -5 & -3 \end{bmatrix}$ and $\theta = \begin{bmatrix} 10 \\ 10 \end{bmatrix}$.

We note that A has poles in the right half plane and hence it is an unstable non-minimum phase system. The constant θ is assumed to be unknown and the compact set can be conservatively chosen as $\Omega = \{\theta_1 \in [0, 20], \theta_2 \in [0, 20]\}$. The control objective is to design an adaptive controller $u_d(t)$ to ensure that $x_1(t)$ tracks any reference signal $r(t)$ both in transient and steady state.

For implementation of the $\mathcal{L}_1$ adaptive controller (3.5), (3.6), (3.7), we need to verify the $\mathcal{L}_1$ stability requirement in (3.10). For constant $\theta = \begin{bmatrix} 10 & 10 \end{bmatrix}^T$, we have

$$A_g = \begin{bmatrix} A_m + b\theta^T & b \\ -k\theta^T & -k \end{bmatrix} = \begin{bmatrix} 0 & 1 & 0 \\ 5 & 7 & 1 \\ -10k & -10k & -k \end{bmatrix}. \tag{4.1}$$

Note that for $k > 50$, the matrix A_g is Hurwitz. We set $k = 100$, which means that the transfer function for the low-pass filter takes the form

$$G_{fil}(s) = \frac{100}{s + 100} = \frac{1}{\frac{s}{\omega_0} + 1}, \quad \omega_0 = 100. \tag{4.2}$$

Figure 3(a) illustrates the bode plot for the transfer function (4.2).

The bode magnitude plot tells us that at the break frequency, $\omega = \omega_0 = 10^2$ rad/sec, the gain is about 3.01 dB and the phase is $-\frac{\pi}{4}$ degree. At lower frequencies, $\omega \ll \omega_0$, the gain is approximatly zero, and at higher frequencies, $\omega \gg \omega_0$, the gain increases at 20 dB/decades and goes through the break frequency at 0 dB; that is, for every factor of 10 increase in frequency, the magnitude drops by 20 dB. We can thus say that the low-pass filter (4.2) we use can pass all signals with frequencies lower than the break frequency 10^2 rad/sec, and attenuates (reduces the amplitude of) signals with frequencies higher than 10^2 rad/sec (Note that 1 Hz=2π rad/sec).

Similarly, we can write the transfer function of the reference model (3.13) as:

$$G_{ref}(s) = \frac{5}{s^2 + 3s + 5} = \frac{1}{\left(\frac{s}{\omega_0}\right)^2 + 2\zeta\left(\frac{s}{\omega_0}\right) + 1}, \quad \omega_0 = \sqrt{5},\ \zeta = h\frac{3}{2\sqrt{5}} \tag{4.3}$$

Figure 3(b) illustrates the bode plot for the transfer function (4.3).

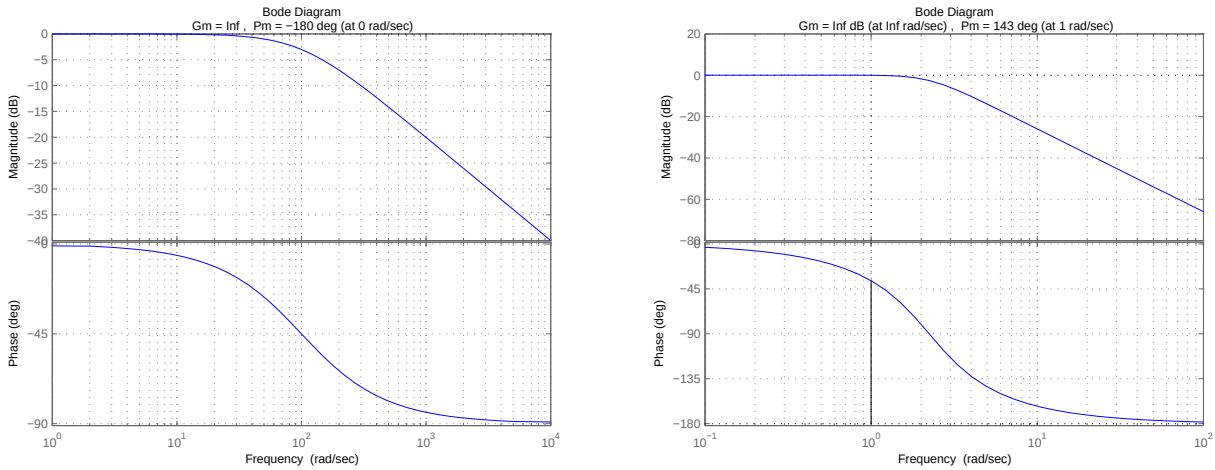

(a) (b)

Figure 3. Bode diagram; (a) Low-pass filter, (b) the reference model.

We can read from the bode magnitude plot that at the frequencies higher than the break frequency, $\omega_0 = \sqrt{5}$ rad/sec, the gain increases at 40 dB/decades and goes through the break frequency at 0 dB; that is, for every factor of 10 increase in frequency, the magnitude drops by 40 dB. At lower frequencies, $\omega \ll \omega_0$, the gain is approximately zero and a peak occurs in the magnitude plot near the break frequency ω_0. The peak has a magnitude of

$$|G_{ref}(j\omega_r)| = -20\lg(2\zeta\sqrt{1-\zeta^2}) = 0.004 \text{ dB} \sim 0$$

where $\omega_r = \omega_0\sqrt{1-2\zeta^2} = 0.7$.

To solve the ODE system $(3.5) - (3.7)$, we consider two techniques: use of the MATLAB routine ode15s and an implicit Euler technique.

4.1. ODE15s

We first consider a single-frequency sinusoidal function $r(t) = \cos(t)$. The frequency of $r(t)$ is $1/2\pi$ Hz $(= 1$ rad/sec), based on the above analysis, this $r(t)$ could pass the filter and reference model unchanged. Theoretically, the tracking output $x_1(t)$ should exactly match the shape of $r(t) = \cos(t)$ after $x_1(t)$ converges. Simulation results are shown in Figure 4(a). We note that the system output $x_1(t)$ converges to $r(t)$ asymptotically whereas $x_1(t)$ lags behind the reference signal $r(t)$ with delay time of about $t_0 = 0.62$ sec. The system output $x_1(t)$ and predictor output $\hat{x}_1(t)$ are almost the same. To cancel out the delay, we could redefine $r(t)$ by $r(t+t_0)$, so it requires that we should have an exact prediction of the time-delay t_0 in advance. The performance for $r(t) = \cos(t)$ with time compensation is shown in Figure 4(b), and we can see that the $x_1(t)$ could exactly track the reference signal $r(t)$ if we have a good prediction of the time delay.

Next, we consider a multi-frequency sinusoidal reference signal $r(t) = 2\cos(t) + 10\cos(\pi t/5)$. We keep the same values for all other parameters. This multi-frequency $r(t)$ could also pass the filter and reference model unchanged. The simulation result shown in Figure 5(a) points out that time-delay is independent of the frequencies of the reference signal $r(t)$; it only depends on the model and controller (low-pass filter) we choose, while a rigorous relationship between the model and time-delay has not been derived yet. The performance for $r(t) = 2\cos(t) + 10\cos(\pi t/5)$ with time compensation is shown in Figure 5(b).

Further, we consider two typical trajectories common to nanopositioning and industrial applications. Simulation results for the trajectories $r_1(t)$ and $r_2(t)$ are plotted respectively in Figure 7 and Figure 8. The results illustrate that the $\mathcal{L}_1$ control design employing homogenized energy model based inverse filters can maintain

a tracking accuracy once cutting commences even though the transducer is operating in the hysteretic and nonlinear regime.

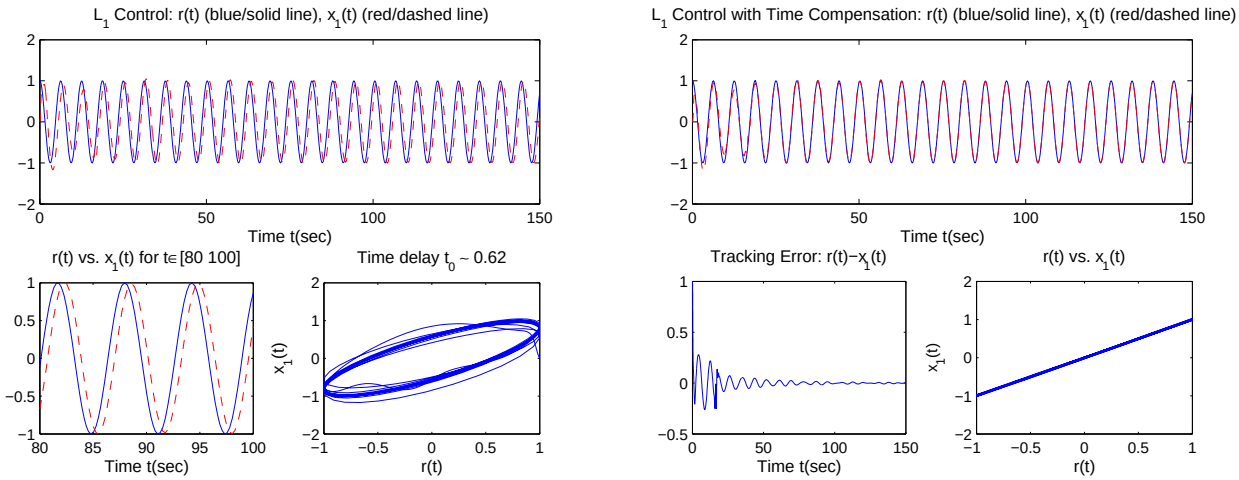

(a) (b)

Figure 4. Performance of $\mathcal{L}_1$ adaptive controller for reference input $r = \cos(t)$ with (a) no time compensation and (b) time compensation.

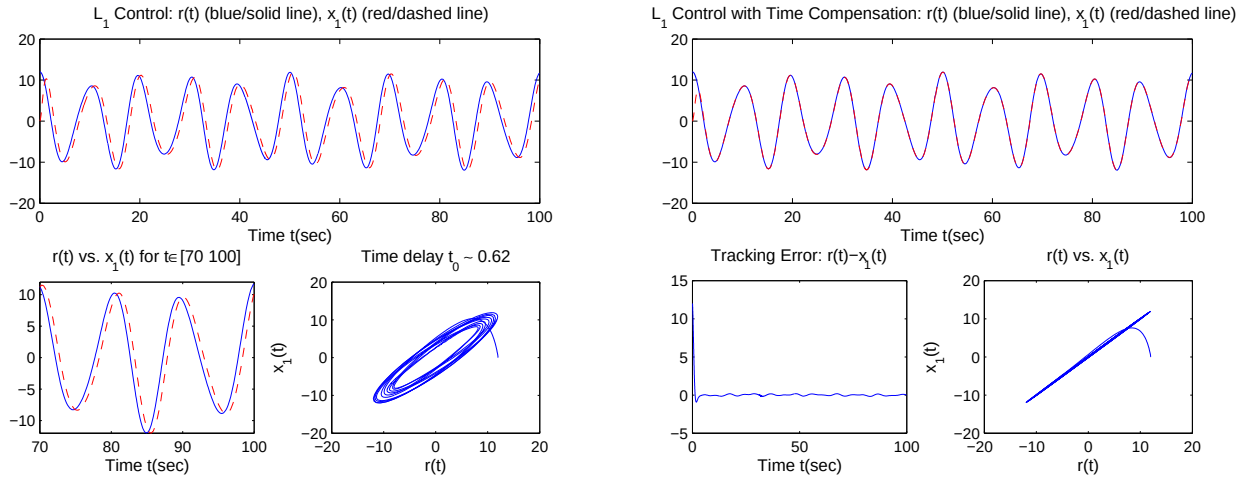

(a) (b)

Figure 5. Performance of $\mathcal{L}_1$ adaptive controller for $r = 2\cos(t) + 10\cos(\pi t/5)$ with (a) no time compensation and (b) time compensation.

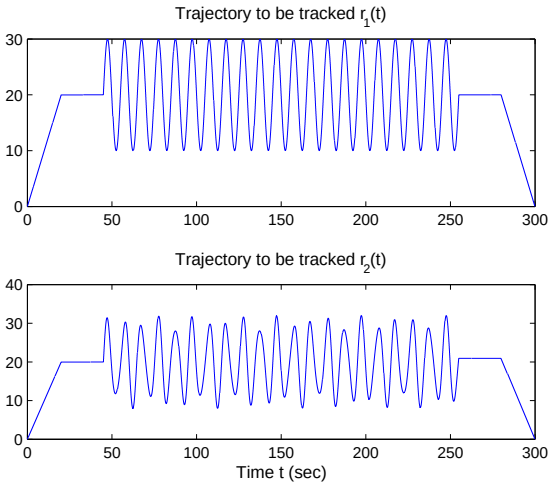

Figure 6. Trajectories to be tracked

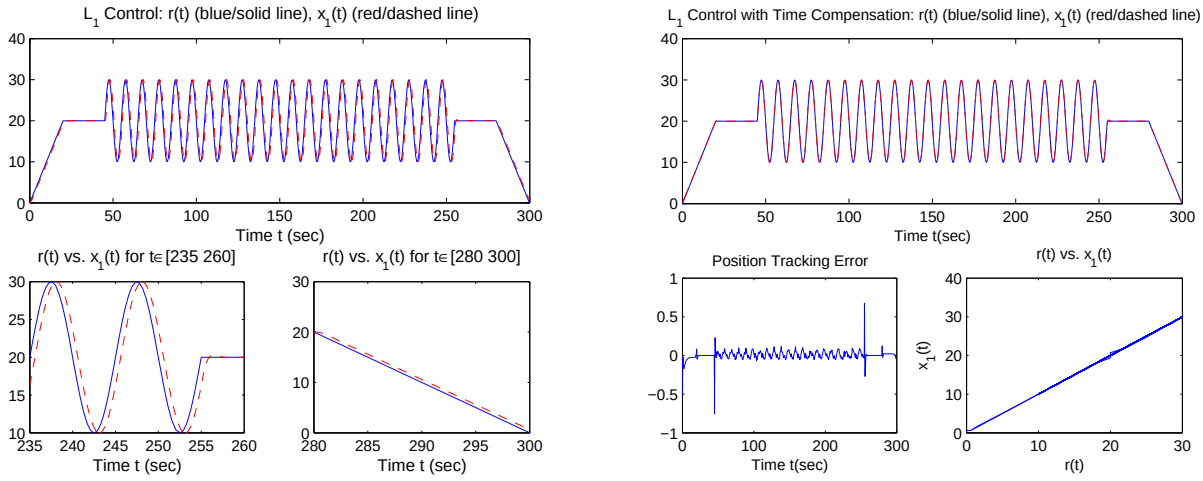

(a) (b)

Figure 7. Performance of $\mathcal{L}_1$ adaptive controller for $r_1(t)$ with (a) no time compensation and (b) time compensation.

4.2. The Implicit Euler Method

Secondly we apply the implicit Euler method to solve the ODE system (3.5) – (3.7). Using the implicit Euler method, we aim to see if it can improve the time delay problem. The simulation results for reference input $r = \cos(t)$ are shown in Figure 9. We can see that the tracking performance is much more stable compared to the results obtained by ODE15s (see Figure 4), but there is no significant improvement in reducing the time delay, and it takes 60% more of CPU time. Next, we apply the implicit Euler method to the same multi-frequency reference signal that we used in section 4.1, i.e., $r(t) = 2\cos(t) + 10\cos(\pi t/5)$. We note that the results, shown in Figure 10, are quite similar to the results we got by using ode15s; which means that, for this $r(t)$, the implicit method doesn't improve very much on the tracking performance, and it's more time consuming and costly. For the reference signals given in Figure 6, the system responses are plotted in Figure 10 and Figure 11.

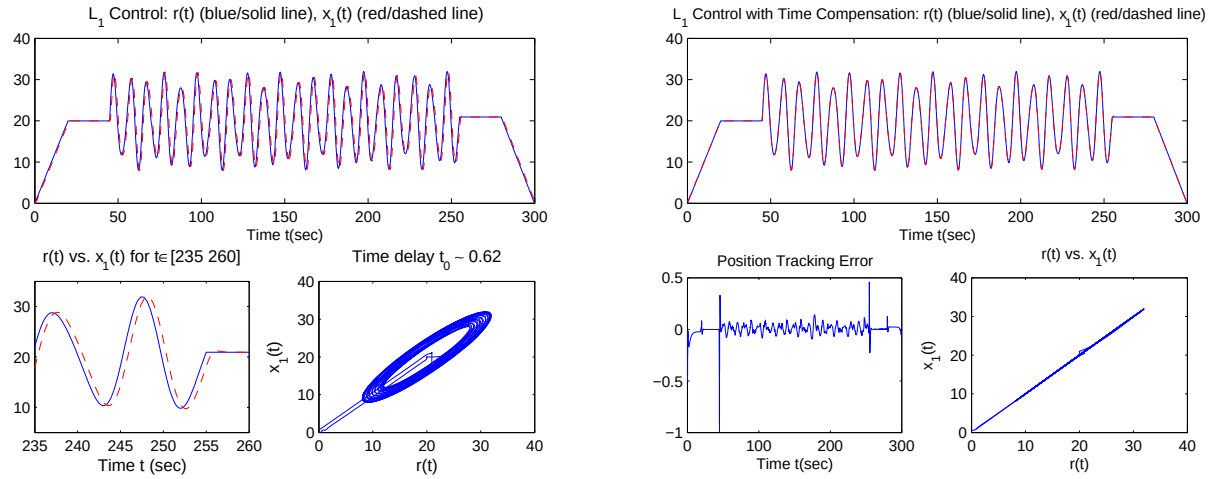

(a) (b)

Figure 8. Performance of $\mathcal{L}_1$ adaptive controller for $r_2(t)$ with (a) no time compensation and (b) time compensation.

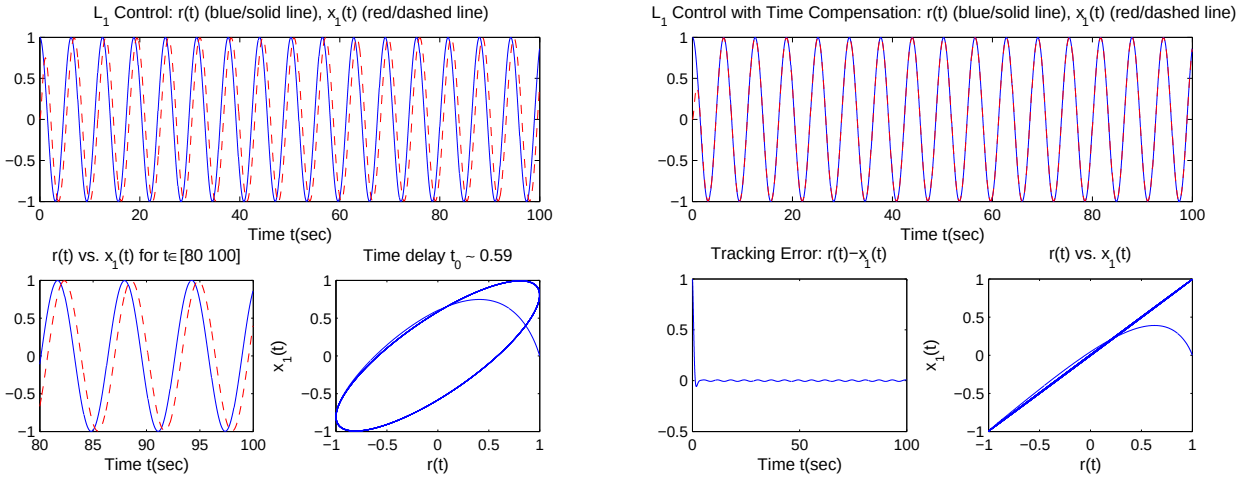

(a) (b)

Figure 9. Performance of $\mathcal{L}_1$ adaptive controller for $r(t) = \cos(t)$ with the implicit Euler method with (a) no time compensation and (b) time compensation.

5. CONCLUSION

A robust control framework was developed by combining the inverse compensation with $\mathcal{L}_1$ control theory. The control design has focused on applications where the reference displacement is known in advance and precise control is desired at relatively high speed. The incorporation of the homogenized energy model in the control design was shown to significantly improve the tracking performance. Simulations of an unstable non-minimum phase system verify the efficiency of the control framework.

ACKNOWLEDGEMENT

This research was supported in part by the Air Force Office of Scientific Research through the grant AFOSR-FA9550-04-1-0203.

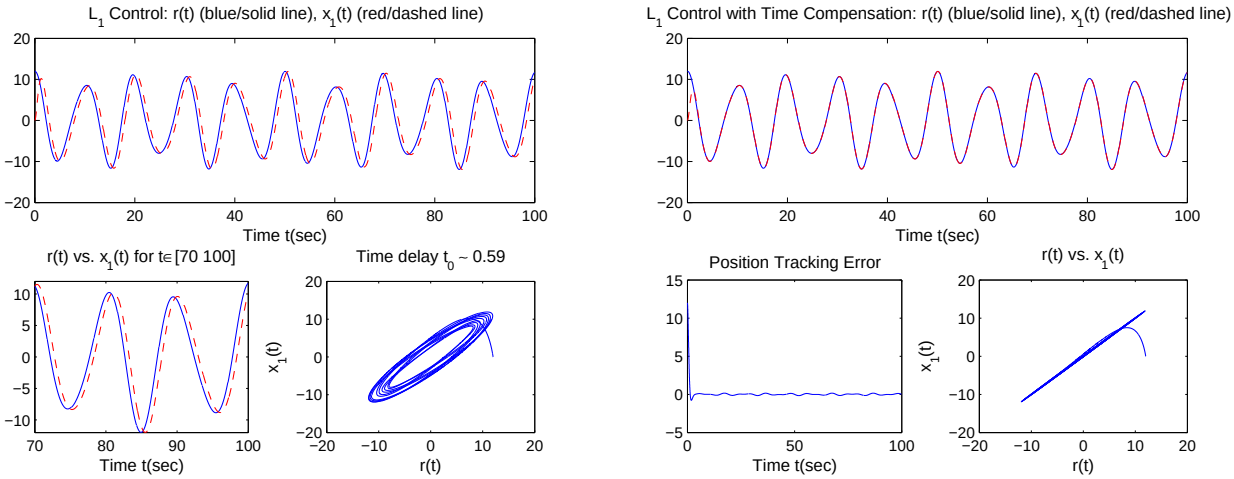

(a) (b)

Figure 10. Performance of $\mathcal{L}_1$ adaptive controller for $r = 2\cos(t) + 10\cos(\pi t/5)$ with the implicit Euler method with (a) no time compensation and (b) time compensation.

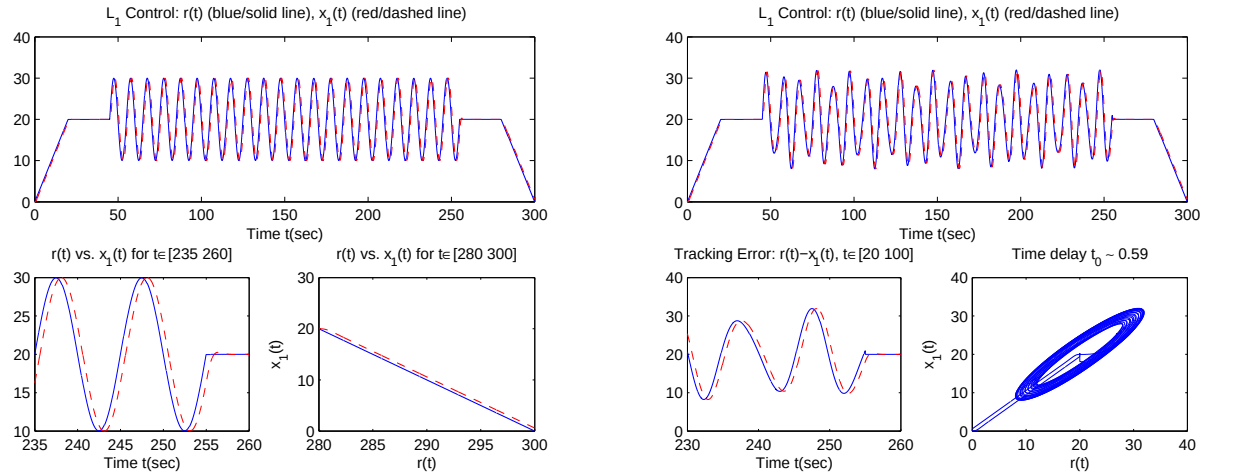

(a) (b)

Figure 11. Performance of $\mathcal{L}_1$ adaptive controller for $r_1(t)$ and $r_2(t)$ with the implicit Euler method with (a) no time compensation and (b) time compensation.

REFERENCES

1. T.R. Braun, R.C. Smith, "Efficient Implementation of Algorithms for Homogenized Energy Models", *Continuum Mechanics and Thermodynamics*, 18(3-4), pp.137-155, 2006.
2. C. Cao, N. Hovakimyan, "Design and Analysis of a Novel $\mathcal{L}_1$ Adaptive Control Architecture with Guaranteed Transient Performance", *Proc. American Control Conference,* 2006.
3. C. Cao, N. Hovakimyan, "$\mathcal{L}_1$ Adaptive Controller for System in the Presence of Unmodelled Actuator Dynamics", *Proc. 46th IEEE Conference on Decision and Control*, 2007.
4. R.C. Smith, " Smart Material Systems: Model Development." Philadelphia, PA: SIAM, 2005.